frontiers | Frontiers in Earth Science

TYPE Original Research
PUBLISHED 09 May 2023
DOI 10.3389/feart.2023.1165809

OPEN ACCESS

EDITED BY
Jian Liu,
Qingdao Institute of Marine Geology (QIMG), China

REVIEWED BY
Xiting Liu,
Ocean University of China, China
Bo Liu,
Alfred Wegener Institute Helmholtz Centre for Polar and Marine Research (AWI), Germany

*CORRESPONDENCE
Ke Cao,
53932214@qq.com

RECEIVED 14 February 2023
ACCEPTED 17 April 2023
PUBLISHED 09 May 2023

CITATION
Sun T, Cao K, Yin P, Jiang X and Tian Y (2023), Authigenic pyrite and gypsum minerals in offshore Zhoushan sediments: morphology, formation, and environmental implications.
Front. Earth Sci. 11:1165809.
doi: 10.3389/feart.2023.1165809

Authigenic pyrite and gypsum minerals in offshore Zhoushan sediments: morphology, formation, and environmental implications

Tiantian Sun[1,2], Ke Cao[1,2]*, Ping Yin[1,2], Xuejun Jiang[1,2] and Yuan Tian[1,2]

[1]Qingdao Institute of Marine Geology, China Geological Survey, Ministry of Natural Resources, Qingdao, China, [2]Laboratory for Marine Geology, Qingdao National Laboratory for Marine Science and Technology, Qingdao, China

Offshore Zhoushan sediments are a potential area for shallow gas resources in China, where authigenic pyrite is widely distributed. Pyrite content, size distribution, and morphology are influenced by depositional conditions and are sensitive to environmental changes. This study investigated the authigenic pyrites or gypsums of core JC-1 offshore of Zhoushan. Scanning electron microscopy was used to observe the pyrites and identify various aggregations. Changes in lithology, chlorine content, and stable isotope values of organic matter were analyzed to indicate the evolution of ancient marine, floodplain estuary, tidal flat environments, and shallow marine sedimentary facies. The morphology and microcrystalline structure of these types of pyrites can be divided into spherical framboid aggregates, sub-euhedral aggregates, and microcrystalline euhedral pyrites with different sedimentary facies. Gypsum minerals and the coexistence of pyrite and gypsum were found in the enriched authigenic pyrites at the SMTZs. The sources of sulfate formed by authigenic gypsums may originate from overlying seawater and pyrite oxidation, whereas calcium ions may come from the dissolution of carbonate or calcareous shells caused by local environmental acidification. The various aggregations of pyrites observed may be related to SO_4-AOM in different environments. The findings suggest that authigenic gypsums form due to local environmental acidification and that the sources of the formed sulfate may be from overlying seawater and pyrite oxidation. This study provides a new perspective for understanding the responses of different sedimentary environments to sea level rise and climate change.

KEYWORDS

authigenic pyrite, gypsum minerals, sedimentary facies, environmental evolution, Offshore Zhoushan

1 Introduction

During early diagenetic processes, a variety of authigenic sulfide minerals are formed in marine sediments; these minerals can be roughly divided into two types: acid volatile sulfur (AVS; AVS=FeS + H_2S + 2/3 Fe_3S_4), mainly composed of iron monosulfide minerals (e.g., mackinawite), and chromium-reducible sulfur, mainly pyrites (CRS; CRS= FeS_2 + S^0 + 1/

3 Fe_3S_4). Overall, unstable iron monosulfide minerals eventually transform into diagenetically stable pyrite (Rickard and Luther, 2007; Taylor and Macquaker, 2011; Lin et al., 2016d; Liu et al., 2020a). The formation of authigenic pyrite in sediments is controlled by a combination of factors, including the degradation of organic matter, the sulfate content in pore water, and the active iron content. Thus, pyrite is an important tool for studying early diagenesis (Jørgensen, 1982; Berner, 1984; Böttcher and Lepland, 2000). Therefore, pyrite in marine sediments is an important sink for sulfur and iron and plays an important role in global C-S-Fe biogeochemical cycles (Berner, 1984; Liu et al., 2020a). Organoclastic sulfate reduction (OSR) is the dominant anaerobic mechanism of organic matter remineralization and sulfide (H_2S) formation, which then reacts with active iron to form iron sulfide and is buried in modern marine sediments (Liu et al., 2021).

Framboids are generally the most common morphological type of authigenic pyrite. They are zoned aggregates with radial overgrowths that surround the framboidal cores, fillings, and agglomerates (Amstutz et al., 1967). Variations in their morphological types reflect the difference between the physical and chemical conditions of the water body during its formation and the later diagenetic environments (Shevelkova et al., 1996). Authigenic pyrite is widely developed on the inner shelves of the Yellow Sea and the East China Sea. Early pioneering research on the distribution, morphological type, formation, and control factors of authigenic pyrite developing in the sea area indicated that its formation process and characteristics are closely related to the sedimentation process and are controlled by different factors, including organic matter content, system openness, anaerobic oxidation of methane (AOM), and sedimentation rate (Kang et al., 2014; Chang et al., 2020; Liu et al., 2022). In addition, pyrite abundance and morphological characteristics may be influenced by local depositional environments, particularly during physical reworking and bioturbation (Richardson et al., 2019; Liu et al., 2022). Therefore, diverse sedimentary environments and geological evolution can be recorded in the content, morphology, and other signals of authigenic pyrite, which provide good materials for studying the response mechanisms of authigenic pyrites to sedimentation environments.

As a typical evaporative salt mineral, authigenic gypsum ($CaSO_4{\cdot}2H_2O$) is widely found in evaporitic environments in arid climate conditions and semi-restricted basins, as well as in non-evaporative deep marine sediments and cold and dry polar environments. The oxidation of sulfides, the action of acidic sulfate solutions on calcareous rocks, and the hydration of anhydrite ($CaSO_4$) are the most common forms of non-evaporative gypsum (Vogel et al., 2010; Haffert et al., 2013; Lin et al., 2016a; Liu et al., 2018b). The coexistence of authigenic gypsum and pyrite was recently reported as a typical mineral assemblage in cold seeps (Lin et al., 2016a; Zhao et al., 2021; Dantas et al., 2022). The formation mechanism of authigenic gypsum is linked to the oxidation of authigenic pyrite and the evolution of the underlying methane seeps. Zhao et al. (2021) suggested that gypsum formation is likely associated with the downward migration of the sulfate–methane transition zone (SMTZ), which causes anaerobic pyrite oxidation at its original site of formation. Liu et al. (2020b) also found authigenic gypsum minerals in a location where a large amount of pyrite was formed in a study of authigenic minerals in EC2005 core samples from the East China Sea shelf. However, the mechanism of authigenic gypsum formation is not well understood. Additionally, authigenic pyrite–gypsum association is rare in marine sediments, mainly in the southwest Indian Ocean (Criddle, 1974), the southwest continental slope of Africa (Siesser and Rogers, 1976), the Madras sea area (Vijaykumar and Vaz, 1995), and Rías Baixas (Garcia-Gil, 2003). Additionally, Chinese researchers have identified gypsum-pyrite assemblages in the sediments of the South China Sea (Chen et al., 2007; Lin et al., 2012), which they suggested was related to Ca^{2+} enrichment caused by the dissolution of carbonate or biological shells by hydrogen sulfide released by the decomposition of organic matter or methane migration.

Offshore Zhoushan had a typical shallow depositional environment. During several transgressions and regressions in the Quaternary, sediments were formed in multiple layers with freshwater and marine sedimentary facies (Lin et al., 2004; Liu et al., 2022), and multiple sets of muddy, silty, and sandy sediments rich in organic matter were alternately deposited (Chen et al., 2020). After the last glaciation, offshore Zhoushan experienced depositional evolution from the river channel to the floodplain estuary and the present estuarine-shallow sea, with an increase in sea level (Lin et al., 2005). Based on recent high-resolution seismic surveys (Figure 1B), biogenic shallow gas (mainly methane) is widely developed in the sediments of offshore Zhoushan, with a water depth of approximately 0–25 m (Ni et al., 2013). Because of the methane, AOM may be the dominant process for sulfide production, which is finally preserved as authigenic pyrites (Liu et al., 2020a). Other researchers have used geochemical methods, mainly AOM and methanogenesis, to study the geochemical characteristics of sediments (He et al., 2020). We recently found abundant pyrites formed in the shallow gas enrichment area offshore of Zhoushan, which are probably related to AOM or OSR. The study of the evolution of the sedimentary environment by tracing differences in pyrite morphology and highly variable content is of great scientific importance because it can provide new ideas and avenues for understanding variable local environmental conditions. For instance, the sedimentary pyrites and C/S ratios of mud sediments on the East China Sea inner shelf indicate a late Pleistocene–Holocene environmental evolution (Liu et al., 2020a; Liu et al., 2022). However, little has been reported on the morphological characteristics and the constraints of authigenic pyrite in the offshore Zhoushan sediments. In this study, we selected, separated, and identified authigenic pyrite and gypsum minerals from sediment samples of core JC-1 in a shallow gas enrichment area offshore of Zhoushan. Combined with a comprehensive study on the total sulfur and grain size of bulk sediments and methane contents in the headspace, we explored the origin of pyrite and gypsum minerals to establish the diagenetic process for the observed morphology signals and their implications for environmental changes during deposition.

2 Materials and methods

2.1 Geological setting

Core JC-1 was located in the coastal area of Zhoushan (Figure 1). Controlled by the regional structure and various

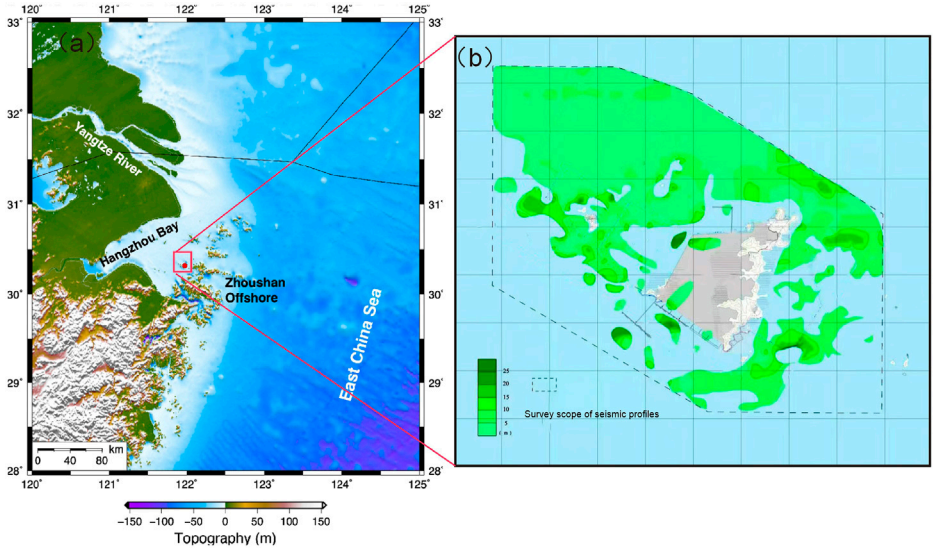

FIGURE 1
(A) Geological background map of the study area showing the location of core JC-1. **(B)** Seismic profile of the shallow gas distribution in the study area.

natural agents in the later stage, the island location in the research area is mainly in the form of long strips and is distributed in the southwest to the northeast direction (Chai et al., 2015). It lies on the inner shelf of the East China Sea (ECS) (Figure 1). The ECS is a typical river-dominated marginal sea characterized by the delivery of large amounts of terrigenous sediments from surrounding rivers, including the Yangtze and Qiantang rivers (Yang et al., 2016; Liu et al., 2018a). The distribution and dispersal patterns of terrigenous sediments in the ECS are modulated by oceanic and tidal currents, as well as sea level, which leads to the formation of variable sedimentary systems on the continental shelf (Liu et al., 2018a). A recent study showed an average preservation efficiency of terrigenous organic matter in the ECS inner shelf of approximately 24.7% ± 4.7% (Wu et al., 2013).

During the Last Glacial Maximum (LGM), the entire ECS inner shelf was exposed and represented a terrestrial fluvial environment (Li et al., 2014) because the global sea level was 120–135 m lower than the present sea level (Liu et al., 2022). With the rapid rise in sea level, transgressive system tracts were formed from 11 to 8 ka BP (Chen et al., 2020) and the incised valleys were filled. Consequently, the tide-dominated estuary face overlaid the fluvial sediments and was covered by a tide-dominated delta face. When the sea level reached its high point at ~7.5 ka (Li et al., 2014), the sedimentary environment evolved from shallow water to the current estuary due to the continuous input of sediments from the Yangtze River and local small rivers. According to the seismic profiles, biogenic shallow gas is widely distributed in the shallow mud sediments in the study area (Figure 1), where the total thickness of the Holocene sediments is >40 m (Lin et al., 2004; Hu et al., 2016; He et al., 2020). Owing to the comprehensive impact of terrestrial and marine material inputs, the sedimentation regime provides a solid basis for calculating the sedimentary indicators related to sedimentary pyrite.

2.2 Sample collection

In 2019, the Qingdao Institute of Marine Geology of the China Geological Survey performed a comprehensive geological survey of the central coastal zone of Zhejiang Province, using rotary drilling technology for coring construction near the Zhoushan offshore, in the ECS continental margin. The JC-1 core with a depth of 63 m below sea floor (mbsf) and a diameter of 108 mm was obtained, with a drilling and coring rate of approximately 100%. The geographical location of the study core is N 30°18′55.54″ and E 121°58′32.20″ (Figure 1). After the sediment core was drilled, it was sectioned, observed, photographed, and described on the deck. The total length of the core column at core JC-1 is 63 m. On the vertical profile, the samples showed a transition from gray-black to brown-yellow-brown from top to bottom, mainly composed of muddy sediments, with clear interlayer boundaries. The core sediment samples collected on the ship and the PVC pipes on the deck were divided into small sections approximately 2 m in length according to the number of times. The two ends were then sealed with plastic caps and tapes and stored in the deck cooler. At the end of the voyage, the samples were transported to the core library of the Qingdao Institute of Marine Geology of the China Geological Survey, where they were continuously sampled at 2 cm intervals. A total of 310 samples were collected.

Gas samples at 2–3-m intervals in the sediments were collected immediately after the core was drilled according to a previously published protocol (Jiang et al., 2023). Specifically, a 50-mL disposable sterile syringe, whose head was removed, was inserted into the sediment core. Then, 35 mL of fresh sediment sample in the syringe was placed into a 50-mL glass vial with a 10-mL sodium chloride saturated solution. The vial was quickly sealed with a butyl rubber stopper and aluminum cap. The sealed glass vials were kept in darkness and sent to the Qingdao Institute of Marine Geology,

FIGURE 2
Sediment core JC-1 collected from offshore Zhoushan. Numbers JC1-1 to JC1-29 represent the number of each core segment from top to bottom.

China, for gas content and stable isotopic composition testing (described in Jiang et al., 2023).

Based on the sedimentary structure and grain size characteristics, four sedimentary zones were identified from the core bottom to the top. In the first sedimentary zone (Zone 1: 55–63 mbsf), the sediments were mainly dark gray and grayish-black. In the second sedimentary zone (Zone 2:40–55 mbsf), the sediments were mainly composed of massive yellowish-brown sands with numerous sand clumps and rusty-brown stains. In the third sedimentary zone (Zone 3:23–40 mbsf), the sediments were composed mainly of massive muddy sediments with a small number of sand clumps and horizontal bedding. In the fourth sedimentary zone (Zone 4:12–23 mbsf), the sediments were mainly composed of dark gray and clayey silt (Figure 2).

2.3 Pyrite identification

Authigenic mineral identification was performed at the laboratory at the Qingdao Institute of Marine Geology. An appropriate amount of the sample was fully immersed in water. The dispersed sediment sample was then placed in a water sieve with a 0.063 mm diameter and rinsed repeatedly with distilled water to separate clay and other components with particle sizes <0.063 mm. After drying the washed debris (mainly authigenic minerals, terrigenous debris, and biological shells) in a 60-C incubator for 24 h, the light and heavy minerals were separated with tribromomethane ($CHBr_3$, density is 2.89 g/mL) as the medium. After drying and weighing, the authigenic minerals were observed under a solid-state microscope and manually selected. The extracted authigenic pyrite was sectioned and observed under an optical microscope.

Representative minerals were selected for scanning electron microscopy. We secured a properly sized sample to the metal table with a conductive adhesive and observed the morphology on the machine after carbon spraying. The scanning electron microscope instrument used in this study was obtained from the test room at the Qingdao Institute of Marine Geology. The thermal field emission scanning electron microscope manufactured by a Japanese company was Hitachi S4800, equipped with a Brooke Quantax-200 energy spectrum. The test conditions were as follows: working distance: 8.5 mm; voltage: 15 kV.

2.4 Grain size analysis

Approximately 0.5 mL of bulk sediment was used to digest the organic matter fraction for grain size analyses. Excessive H_2O_2 solution was removed by heating and evaporation before 0.5% of sodium hexametaphosphate was added to completely disperse the sample. Finally, $Na_4P_2O_7{\cdot}10H_2O$ was added to each sample before measuring to prevent aggregate formation. The grain size was measured using a laser particle size analyzer (Mastersize-2000, Malvern Instruments Ltd., United Kingdom) at the Qingdao Institute of Marine Geology, China Geological Survey. The volume percentages of the sand (63–2000 μm), silt (4–63 μm), and clay fractions (<4 μm) were calculated.

3 Results

3.1 Morphology and mineralogy of authigenic pyrites

Most of the handpicked pyrite particles (aggregates with particle sizes >0.063 mm) from the core sediments were the most common authigenic minerals in the shallow gas enrichment area offshore of Zhoushan. The most common morphological types of pyrite aggregate observed under SEM were tubular, cubic, irregular, and spherical and filled with the shells of foraminifera and other organisms (Figure 3). The pyrite shapes and particle sizes varied significantly among the different layers. Overall, the particles were mainly spherical aggregates with a smaller diameter in Zone 4 (12–23 mbsf; Figures 3D, F) and tubular shapes with variations in both diameter and length in Zone 3 (23–40 mbsf; Figures 3A–C). In the deep zone of Zone 1, the pyrite mainly formed irregular aggregates with euhedral crystals (50–63 mbsf). The authigenic pyrite particles had a black metallic luster, a few particles in different zones were fragile, and the internal fresh section was red, which may have been related to pyrite oxidation. Careful SEM observation of the authigenic pyrite-filled foraminiferal shells revealed carbonation in most of the shells (Figure 3). While some foraminiferal shells contained only scattered spherical authigenic pyrite, others had their outer circumference tightly wrapped in spherical shapes, with no growth holes observed in the shell, for smoother flow.

The SEM-EDS analysis of selected parts of the handpicked pyrites showed variable shapes (Figure 4). In general, authigenic pyrite particles consist of finer crystals and have a variety of crystal forms, including spherical, sub-euhedral, and euhedral.

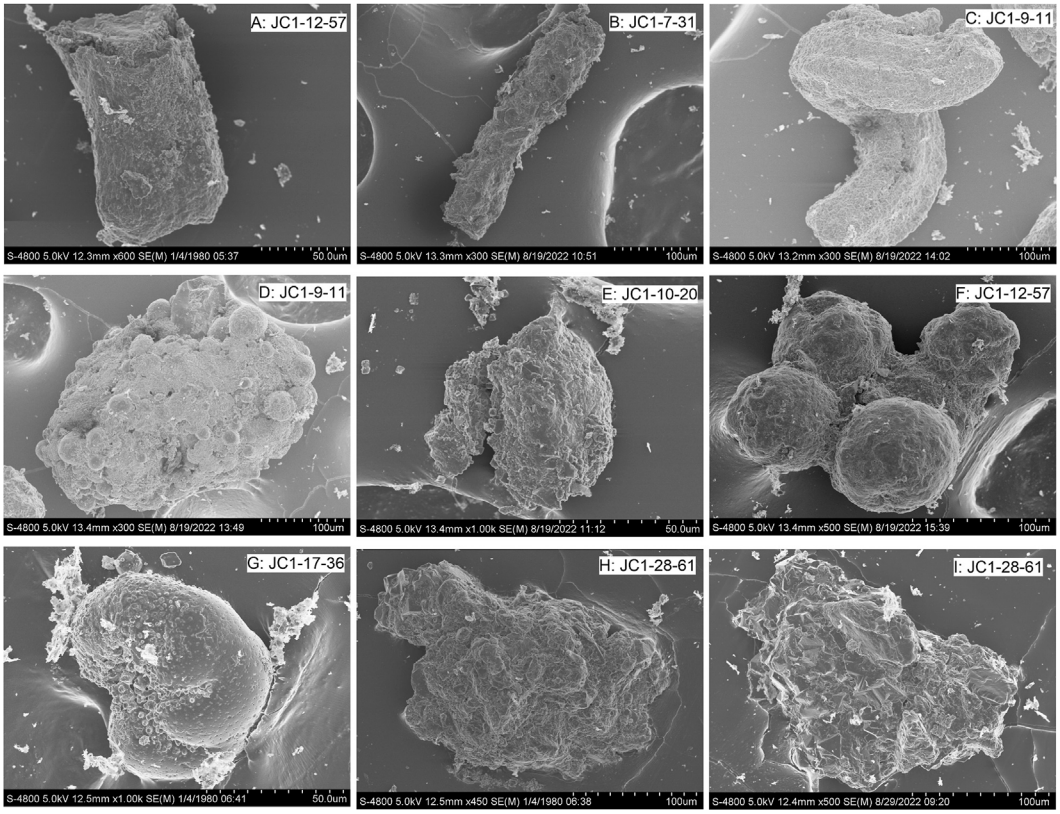

FIGURE 3
SEM micrographs of the morphology of pyrite aggregation in the JC-1 site. **(A)** Long strip pyrite aggregates. **(B)** Selected SEM photographs of authigenic pyrite tubes. **(C)** Curved rod-shaped pyrite. **(D)** Pyrite aggregate formed by the polymerization of spherical pyrite. **(E)** Well-developed pyrite framboids. **(F)** Pyrite aggregate formed by the polymerization of spherical pyrite. **(G)** Foraminifera-filled pyrite aggregates. **(H)** Well-developed pyrite framboids with euhedral microcrystals. **(I)** Accretive pyrite aggregates formed by the disorderly accumulation of numerous octahedral microcrystals.

The irregular aggregates are composed of euhedral-shaped microcrystals approximately 40 μm in size (Figure 4B). In the same spherical and pyrite framboids, the size and diameter of microcrystals are relatively uniform, but the particle size of different framboids varies widely, from about 0.1 to 4 μm (Figures 4C, F–I). The observation results in multiple zones of core JC-1 showed certain differences in the aggregate and crystal morphologies of authigenic pyrite in different layers. The massive tubular pyrites were composed of pyrite framboid and sub-euhedral crystals approximately 20–40 μm in size (Figures 3A–C; Figures 4F, I). Overall, they presented a tree-like shape, indicating that they were microchannels for fluid migration in sediments (Figures 3A, E). Morphologically, pyrite framboid crystals of uniform size continued to grow from the pores, making the structure more compact and showing the growth characteristics of different periods.

EDS spectra were used to test the authigenic pyrites selected under a microscope for some individuals. The results showed two distinct narrow Fe and S peaks, with a mass content almost completely coincided with the standard peak spectrum of FeS_2 (Figure 5; Figure 7). The EDS mode may have experienced elemental interference from the surrounding matrix or other minerals during the pyrite analysis; thus, other elements such as oxygen (O) and silicon (Si) could have been captured in the EDS spectra. The pyrite particles in the same sample were observed under a scanning electron microscope. Therefore, while authigenic pyrite particles were present in the sediments, their content distribution was uneven at different depths.

3.2 Gypsum morphology and the coexistence of authigenic gypsum and pyrite

In addition to pyrite, gypsum was a relatively common authigenic mineral in the core JC-1 sediments in the study area. Most of the gypsum crystals handpicked from the core sediments were aggregations of granular spherical shapes, and some coexisted with authigenic gypsum and pyrite (Figures 6D–G). The gypsum crystals were mainly in the form of microspheres and elongated rod-shaped gypsum and were mostly distributed as rosette clusters or aggregates. The SEM-EDS results of the gypsums (Figure 7) showed that the rosette clusters were mainly composed of Ca, O, and S, which are the spectral peaks of gypsum. In addition to authigenic gypsum, irregular and massive authigenic carbonates (Figure 7) were also found on the large granular pyrite. The particles often showed a flat crystal surface, about 100 μm in size.

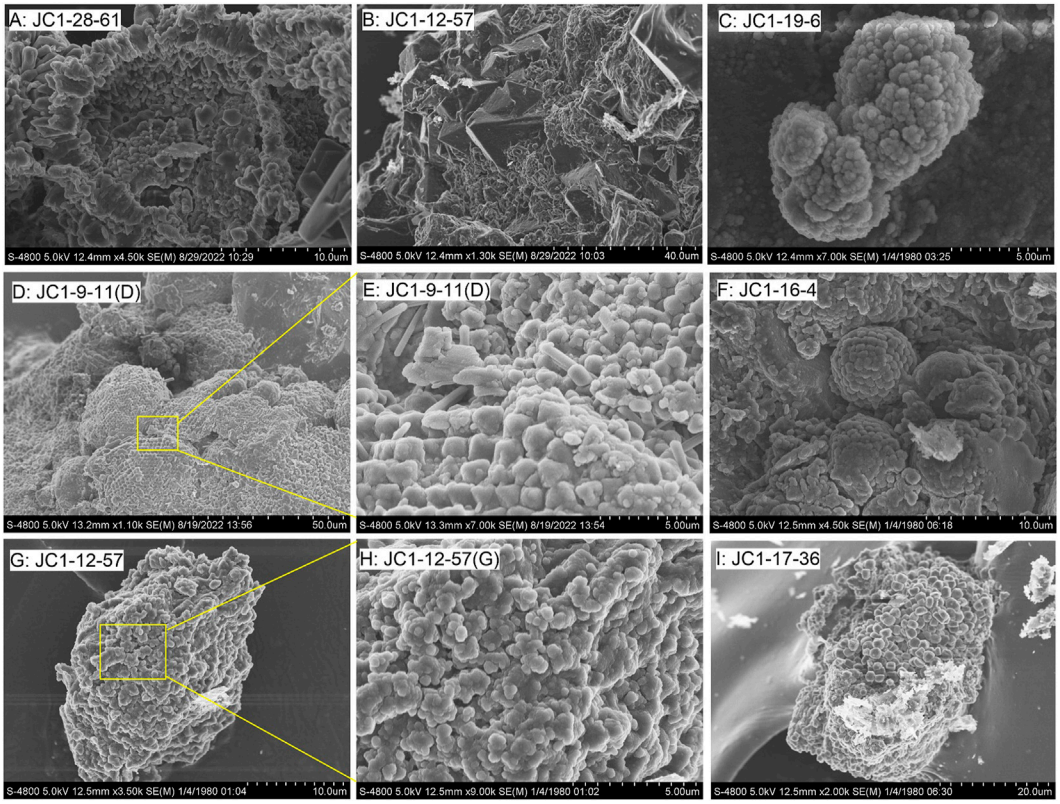

FIGURE 4
Selected SEM photographs of authigenic pyrites. **(A)** Pyrite pyritohedron with a spherical framboid in the center. **(B)** Well-developed pyrite framboids with octahedral microcrystals. **(C)** Well-developed pyrite framboids. **(D)** Euhedral pyrite. **(E)** Enlarged view of the box in **(D)** showing octahedral pyrite and surrounding elongated pyrite microcrystals. **(F)** Spherical pyrite growing around framboid pyrite. **(G)** Framboid pyrite aggregates. **(H)** Enlarged view of the box in **(G)**. **(I)** Well-developed pyrite framboids with euhedral microcrystals.

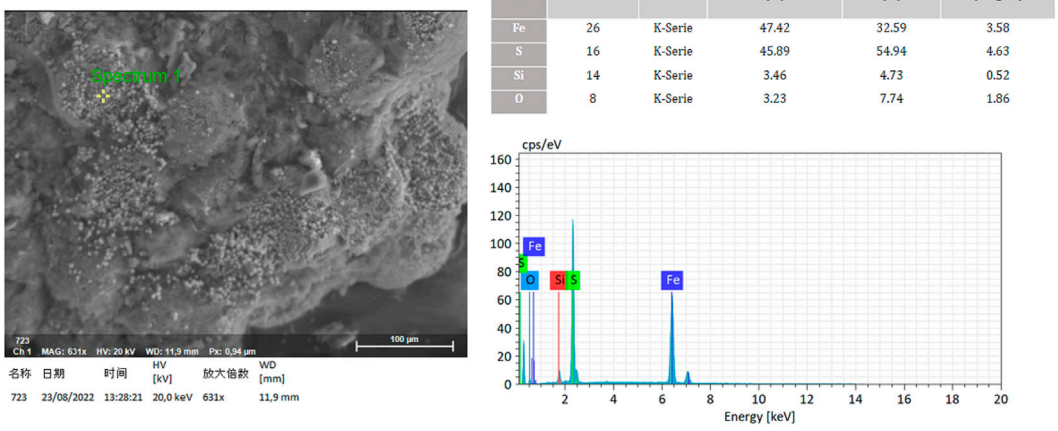

FIGURE 5
EDS analysis of pyrite showing Fe and S at the major content (sample number JC1-12-57).

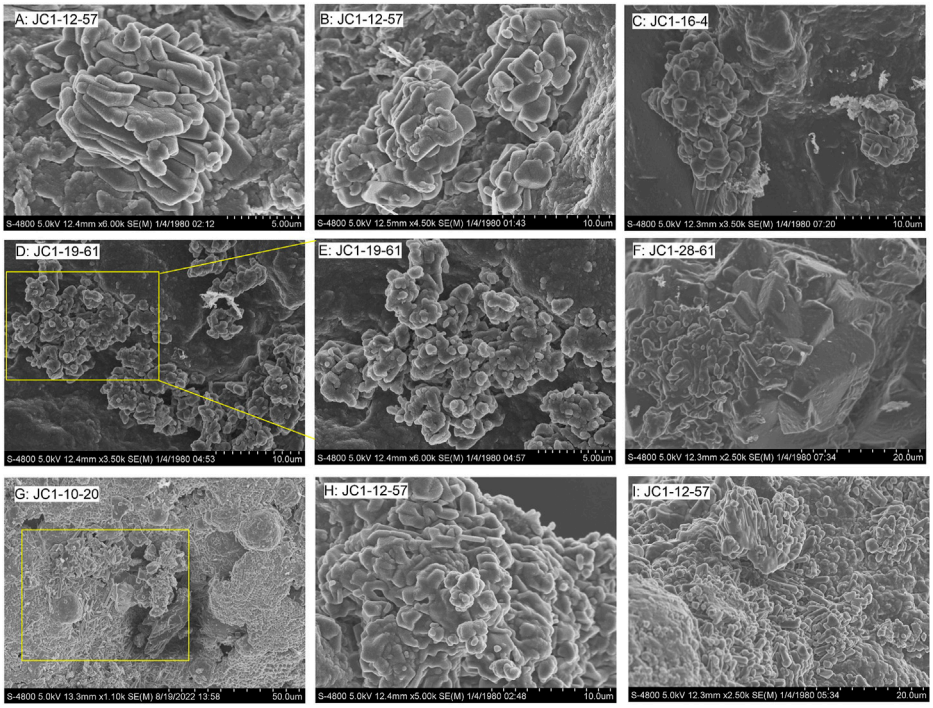

FIGURE 6
Morphology of gypsum from the JC-1. **(A)** Elongated rod-like gypsum aggregates. **(B)** Spherical and elongated rod-shaped gypsum aggregate. **(C)** Cluster-like gypsum aggregate. **(D)** Cluster-like gypsum aggregates. **(E)** Enlarged diagram of the box in the figure showing rosette clusters. **(F)** Tufted gypsum and pyrite growing around an octahedron. **(G)** Cluster-like gypsum growing around spherical pyrite. **(H)** Rosette forming pyrite–gypsum symbiosis. **(I)** Elongated rosette gypsum aggregates.

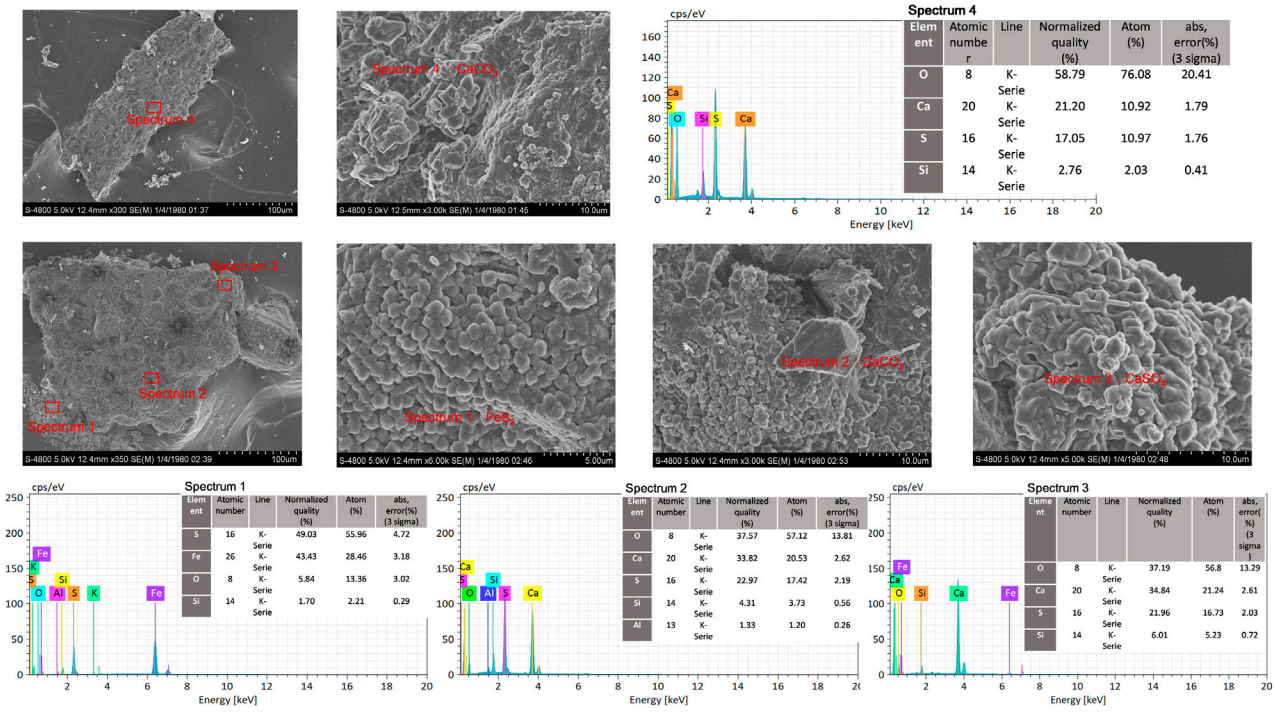

FIGURE 7
Microcrystal morphology and structure characteristics of pyrite–gypsum intergrowth in the sediments of the study area and energy spectrum (EDS) analysis of gypsum showing that its main chemical components are Ca, O, and S. The irregular and tubular pyrite are from samples JC1-10-20 and JC1-28-61, respectively.

3.3 Pyrite content and gypsum distribution

In this study, the sediment samples were first pretreated by sieving and washing. Authigenic minerals were then identified and selected under SEM. Some samples showed the presence of gypsum particles. Because almost all of the samples were consumed, it is difficult to analyze the content of the gypsum particles in the sediment using chemical methods. Therefore, in this study, the presence of gypsum was observed using SEM and verified by EDS. We observed gypsum in five samples from core JC-1 (Figure 9), with a distribution of 17–20 mbsf, 31 mbsf, 38 mbsf, and 61 mbsf. The coexistence of pyrite and gypsum was also found at the 17.5 mbsf, 38 mbsf, and 61 mbsf depths.

The relative contents of hand-picked pyrite in coarse-grained heavy minerals (>63 μm) are shown in Figure 9 and Supplementary Table S2. Pyrite is in high abundance at ~17 bmsf, ~39 bmsf, and ~60 bmsf. The pyrite contents increased significantly (0.76 wt.%) at 17.5 mbsf, followed by a decrease to a low value (0.09 wt.%) at 30.9 mbsf. The relative pyrite contents then increased again, up to 0.58 wt.% at 37.8 mbsf, before finally dropping to low values (0.02 wt.%). Generally, the relative contents of pyrite within the coarse fraction remained at high abundance in the deeper portion of 59–62 mbsf.

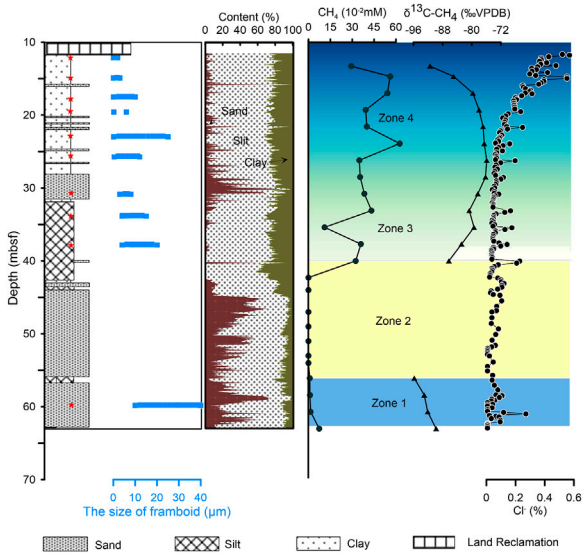

FIGURE 8
Lithological distribution of the sediment core from JC-1.

4 Discussion

4.1 Characteristics of pyrite induced by the anaerobic oxidation of methane

The diagenetically stable pyrite in marine and freshwater sediments has a widespread distribution, making it an essential indicator of local environmental conditions. This is due to the varying pyrite morphologies, high content, and variable sulfur isotopic compositions observed in different sediment (Lin et al., 2017; Rickard et al., 2017; Liu et al., 2019; Miao et al., 2021; Liu et al., 2022). The morphological characteristics and crystal shapes of pyrite are controlled by the nature of the supersaturated conditions, which vary between different pathways of pyrite formation (Shevelkova et al., 1996; Taylor and Macquaker, 2011; Rickard, 2012).

The high reactive Fe content in this study are shown in Figure 9 and Supplementary Table S1 facilitated the formation of early diagenetic authigenic pyrite during and after sediment deposition. The significant peaks of total sulfur (TS) and pyrite content in the samples suggest that the coarse fraction's relative pyrite content was the primary inorganic sulfide in the sediments are shown in Figure 9 and Supplementary Table S1. The offshore core JC-1 in Zhoushan contained a considerable amount of framboidal pyrite, which occurred as spheroidal, cubic, irregular particles, and tubular or rod-shaped monomers. These pyrite characteristics resemble those of authigenic pyrite reported in the sediments of the East and Yellow seas (Chen, 1981; Chang et al., 2020). Nevertheless, the pyrite morphology and size varied significantly at different depths. For instance, at 60 mbsf in Zone 1 of core JC-1, framboid overgrowth was observed, with a framboid mean size of >20 μm. This suggested that the pyrite framboids formed during the earliest stages of diagenesis (Richardson et al., 2019). In strongly reduced environments, authigenic pyrite often has unique morphological features, such as a long growth time, and it mostly occurs as large framboidal pyrite aggregates or organism-filling aggregates (Miao et al., 2021). Therefore, the mean size and shape of the pyrite particles may suggest that the pyrites in Zone 1 were early diagenetic framboids that precipitated under reduced conditions. Similar findings were observed in Zones 4 and 3. As shown in Figure 7, the mean size of the framboid particles gradually decreased from Zone 3 to Zone 4, accompanied by a gradual transition from tubular or rod-shaped pyrite to smaller spherical particles. Additionally, most of the pyrite particles in the two zones were smaller and had a relatively wider size distribution at 17.5 mbsf and 37.8 mbsf, reflecting an anoxic environment with strongly reduced conditions. The formation of authigenic pyrite in the mud sediments of the East China Sea (Liu et al., 2020a) and the northern continental slope of the South China Sea (Lin et al., 2016b; Lin et al., 2016c) is associated with methane fluids. Given the widespread distribution of biogenic CH_4 offshore of Zhoushan (He et al., 2020), the authigenic pyrite may have formed during early diagenesis via the SO_4-AOM pathway in an anoxic environment.

According to the investigation and analysis of shallow gas data in the study area, free CH_4 gases with extremely low $\delta^{13}C$-CH_4 values (all < - 72 ‰ VPDB) were seen at 12–40 mbsf and 55–63 mbsf shallow gas-bearing layers in the sediments of core JC-1 are shown in Figure 8 and Supplementary Table S2. In this case, methane gas in the sediments underwent SO_4-AOM in the SMTZ, resulting in framboidal pyrite formation. A large amount of framboidal pyrite composed of microcrystals with relatively wider size distributions was observed at 17.5 mbsf, 37.8 mbsf, and 60 mbsf layers, which is considered to be an effective indicator of SMTZ positions (Miao et al., 2021). Microbial methanogenesis of organic matter in the mud sediments produced biogenic methane, which has been vertically distributed in multiple layers within a hundred meters of the seabed during the Holocene and late Pleistocene (Chen et al., 2004; Hu et al., 2016). Since the Quaternary, the sedimentation rate of estuarine

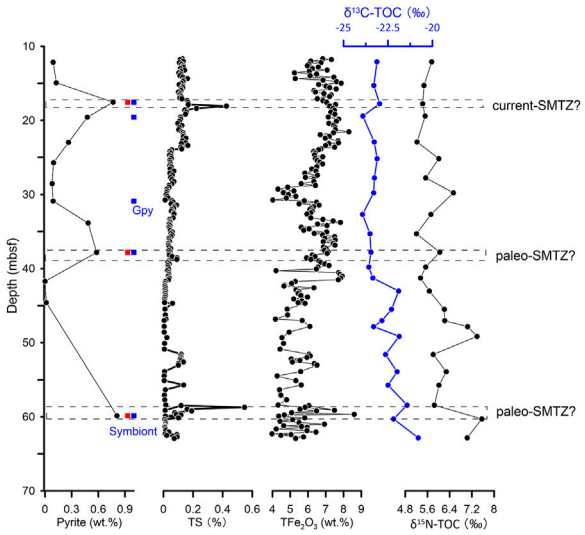

FIGURE 9
TS, TFe_2O_3, and relative content of pyrite in hand-picked coarse-grained (coarser than 63 μm) heavy minerals, and the stable isotopes values of organic matter (δ^{13}C-TOC and δ^{15}N-TOC) in sediment from core JC-1.

facies in the coastal areas of the Qiantang River and offshore Zhoushan has been 4–5 mm/a and has been a long-term process of stable sedimentation. This continuous and rapid sedimentation leads to the sufficient and sustained production of biogenic methane in sediments (Chen et al., 2004). Moreover, multiple transgression-regression processes during the geological history period have made the sediment pore water in the study area rich in certain sulfate concentrations (Li et al., 2014; Dong et al., 2018; Liu et al., 2020a), with a multilayer distribution, providing a material basis for the SO_4-AOM of biogenic methane in the sediment. As a result, extensive development of framboid pyrite occurred in multiple SMTZs and was deposited in the sediment, resulting in large and variable early diagenetic framboid deposits.

The sediments of core JC-1 were also rich in gypsum. The results of the statistical analysis showed that gypsum was mainly enriched in the methane gas-bearing zones. The gypsum enrichment positions were located near or below the pyrite enrichment positions, which were closely associated with pyrite (Figure 6; Figure 9). In the sedimentary environment of core JC-1, the gypsum in the sediments cannot be the result of evaporation. The research core was located offshore of Zhoushan, with a water depth of approximately 60 m. Based on the stratigraphic distribution of gypsum, gypsum was not found in any of the samples with pyrite. In addition, because of the low-temperature preservation environment after core column collection, gypsum crystals could not form during sample processing and sediment storage in core JC-1 (Lin et al., 2016a; Liu et al., 2018b). The gypsums exhibited good self-shaped crystals under SEM. The crystal surface was complete and smooth, had a relatively stable aggregate shape, and did not exhibit obvious wear or erosion (Figure 6), indicating that the gypsum crystals were *in situ* (Vogel et al., 2010; Lin et al., 2016a). Most importantly, we found that the aggregate shape characteristics of gypsum differed in the JC-1 sediment at different depths; some were individual rosette clusters, while others were wrapped with pyrite to form the coexistence of pyrite and gypsum. The differences in gypsum crystal morphology may be related to the speed of mineral precipitation or differences in the chemical conditions in local microenvironments (Vogel et al., 2010; Haffert et al., 2013).

4.2 Sedimentary environmental factors

Sea-level change is the primary driver of changes in the evolution of Late Pleistocene and Holocene shelf environments (Lambeck et al., 2014; Li et al., 2014; Dong et al., 2018; Liu et al., 2022). During the Last Glacial Maximum (LGM; 26.5–19.0 ka), the entire ECS inner shelf was exposed and represented a floodplain–estuary environment due to the lowest sea level (Li et al., 2014). Sea level rise after the LGM (23–15.4 ka) led to the gradual inundation of continental shelf areas worldwide (Lambeck et al., 2014; Li et al., 2014), followed by a rapid sea-level rise during 14.0–12.9 ka in the ECS inner shelf (Dong et al., 2018). The Younger Dryas (YD; 12.5–11.5; Lambeck et al., 2014) was a dramatic cooling event during the transition from the LGM to the Holocene, which led to a transgressive–regressive cycle and represented a tidal flat environment. The global sea-level rise during the last deglaciation (15.4–7.0 ka) oscillated but has slowed since 7.0 ka, as documented in the sediments of the ECS (Liu et al., 2021). The offshore area of Zhoushan is one of the major estuaries along the ECS, where abundant shallow gas reservoirs have been developed (Figure 1; Chen et al., 2004; He et al., 2020). Based on previous studies (Lin et al., 2004; Lin et al., 2010), the 63-m-long sediment core was divided into four sedimentary facies, or zones (ancient marine, floodplain-estuary, tidal flat environment, and present shallow marine), according to the changes in lithology and geochemical data (Figure 7). In Zone 1, a certain amount of elemental chlorine (Figure 8) indicated a marine environment. The lithological characteristics of Zone 1 are dominated by dark gray and grayish-black sediments (Figure 2; Chen et al., 2004), indicating that the Late Pleistocene strata are in a sulfidic environment and have good conditions for microbial methanogenesis. Researchers have frequently employed stable isotopes of δ^{13}C-TOC and δ^{15}N-TOC to differentiate terrestrial and marine organic matter sources (Middelburg and Nieuwenhuize, 1998; Wu et al., 2007; Yuan et al., 2017). The higher δ^{13}C-TOC (−21.7‰ on average) and δ^{15}N-TOC (6.6‰ on average) values in Zone 1 indicated a greater proportion of marine organic carbon (C4) inputs (Yuan et al., 2017; Liu et al., 2020a), which also corresponded to a marine sedimentary environment. Sulfate is a major salt in marine sediments, and anaerobic sulfidic conditions are conducive to the occurrence of SO_4-AOM, resulting in pyrite formation. We found more abundant hand-picked pyrites with high TS and wider size in Zone 1 (Figure 9), which represented an indicator of the marine environment. During the SO_4-AOM process, the HS^- product reacts with reactive Fe in the sediment to produce FeS and release H^+, which in turn is converted to pyrite. H^+ enrichment dissolves carbonates or biological shells, resulting in the enrichment of Ca^{2+} ions.

Therefore, when combined with sulfate in pore water in a marine environment, gypsum precipitates, which also occurs with

pyrite. Based on the pyrite and gypsum content and the existence of pyrite and gypsum, the paleo-SMTZ (~60 mbsf) can be inferred. In Zone 2, the sediments were mainly composed of massive yellowish-brown sands with many sand clumps and rusty-brown stains, which are typical features of the floodplain–estuary deposits. Furthermore, the seawater chlorine content decreased to a relatively stable level, as was also indicated by the floodplain–estuary deposits. We also noticed that the lithological characteristics and grain sizes from Zone 1 to Zone 2 experienced retrogressive aggradation as recorded in the sedimentary sequence, with progressively yellowish, coarse grains (Figure 2). The δ^{13}C-TOC (−22.5‰ on average) and δ^{15}N-TOC (6.2‰ on average) values in Zone 2 indicated a more significant proportion of terrestrial organic carbon inputs. The stable isotope values of terrestrial and marine organic matter overlap over a large range (Wu et al., 2007). Therefore, during the Zone 2 stage, core JC-1 sediments experienced a transition from a marine environment to a terrestrial environment due to sea-level changes during the LGM (Li et al., 2014; Liu et al., 2022), which can be divided into a transgressive lag and a floodplain estuary. Changes in sedimentary environments characterized by varying inputs of terrestrial matter and the presence of coarse sand sediments can be used to infer predictable changes in the quality of organic matter (Sun et al., 2020). Based on the absence of methane, low levels of TS content, and nearly imperceptible pyrite (as shown in Figure 9), the organic matter in this zone can be inferred to consist of refractory organic matter, which is more resistant to decomposition compared to marine sources (Zhao et al., 2021; Liu et al., 2022).

During the end of deposition in Zone 2, the intrusion of seawater began to affect the study area, as evidenced by the multiple peaks in chlorine content (Lambeck et al., 2014; Li et al., 2014). The stable isotope values of organic matter (δ^{13}C-TOC and δ^{15}N-TOC) suggest a mixture of marine and terrestrial sources in the sediments during this period. In Zone 3, the lithological characteristics consist of massive mud sediments with a few sand clumps and horizontal bedding, which indicate tidal facies. Previous research showed that the study area receives significant terrestrial inputs from rivers such as the Yangtze and Qiangtang rivers, with an ample supply of reactive iron (Sun et al., 2020; Zhao et al., 2021; Chang et al., 2022). The presence of abundant iron oxides did not restrict the formation of sedimentary pyrite (Figure 9). With the appearance of hand-picked pyrite aggregates and seawater intrusion, microbial sulfate reduction may have been limited during transgressive intervals. However, gypsum minerals (Figure 8) were also identified, possibly related to the oxidation of authigenic pyrites (Liu et al., 2018b; Zhao t al., 2021). Although seawater is unsaturated relative to gypsum in Zone 3, various processes can lead to increased Ca^{2+} and SO_4^{2-} in pore water. Iron sulfide oxidation is a relatively common process that can lead to an increased sulfate content of pore water (Liu et al., 2018b). Based on the sedimentary structure and grain size characteristics of core JC-1, horizontal stratification was relatively obvious without significant bioturbation or strong physical reworking in Zone 3. Simultaneously, the presence of many tubular pyrites indicates underflow activities such as methane diffusion (Figure 3). The sedimentary environment is mostly anaerobic, and the anaerobic oxidation of deposited iron sulfides (Zhao et al., 2021) and the disproportionation reaction of S intermediates (Pirlet et al., 2010) predominantly affect pore water SO_4^{2-}. Simultaneously, the anaerobic oxidation of deposited iron sulfides can lead to the acidification of local pore water, which, in turn, leads to the dissolution of calcareous biological shells (Pirlet et al., 2010; Liu et al., 2018b; Zhao et al., 2021). The increased Ca^{2+} and SO_4^{2-} content jointly promoted gypsum precipitation.

From Zone 3 to Zone 4, the chlorine content diffused from the tidal facies to shallow marine environments with a concave downward decrease (Figure 8). The sea level was relatively stable during the deposition of Zone 4 and the sediments in the marine environment consisted of dark gray and clayey silt with a relatively uniform grain size distribution (Figure 8). However, we noticed that the grain size increased sharply at a depth of ~15.5 mbsf, which may be related to strong physical reworking and surface reclamation of sediments, as demonstrated by the surface sediments with alternating light yellow and dark gray colors. In Zone 4, the TS and handpicked pyrite had relatively high contents, with a peak of ~17 mbsf. The shallow surface sediments of the original seabed did not contain methane before reclamation; however, after reclamation, this layer contained a considerable amount of biogenic methane. The downward infiltration of seawater may have caused the SO_4-AOM to shift upward and become shallow, and the ~17 mbsf position may be the current SMTZ position. In general, the handpicked pyrites were mainly spherical aggregates with smaller diameters and narrow size distributions, which may also support our speculation that authigenic pyrite was newly formed at the current SMTZ position (Zhao et al., 2021). We also found some gypsum particles and the coexistence of pyrite and gypsum at ~17 mbsf (Figure 8), which may be related to AOM (Dantas et al., 2022). However, the mechanism of sufficient SO_4^{2-} provided by diffusing from the overlying seawater and sulfide oxidation, leading to gypsum formation, cannot be ruled out (Liu et al., 2018b). Therefore, the use of multiple indicators, such as stable S and O isotopes, is recommended to reveal the formation mechanisms of sedimentary authigenic minerals.

4.3 Evolution mechanism of authigenic pyrite and the coexistence of pyrite and gypsum

Love and Amstutz (1966) suggested that pyrite framboid was the main form of pyrite in the early diagenetic stage. Due to changes in environmental conditions, they may further grow and evolve into euhedral crystals in later stages; the specific evolution sequence can be expressed as spherical → sub-euhedral → microcrystalline euhedral → euhedral pyrite. Analysis of the distribution of authigenic pyrite, gypsum, and methane in core JC-1 showed that the morphological characteristics of authigenic pyrite represent the sedimentary evolution process. The coexistence of authigenic pyrite and gypsum may be related to the distribution and migration of shallow gases. Additionally, authigenic gypsum forms as a result of contributions from both seawater and pyrite oxidation, while Ca^{2+} is derived from local seawater acidification due to the oxidation process of authigenic pyrite. Therefore, we propose a simple depositional evolution model for offshore Zhoushan, which explains the formation process of authigenic pyrite and gypsum at the research site since the LGM (Figure 10).

(a) Mud sediments were deposited offshore in Zhoushan before changes in sea level and inland climate. Methanogenesis in mud sediments released a large amount of biogenic methane that

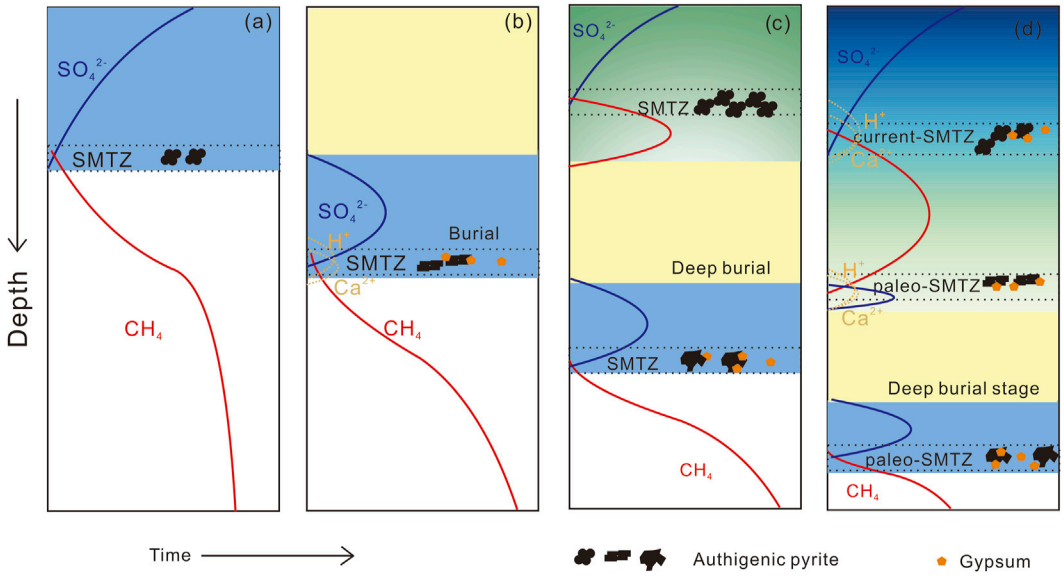

FIGURE 10
Simple diagenetic model for authigenic pyrite and gypsum precipitated in the JC-1 core. No scale reference. **(A–D)** Represent different depositional stages. Black dotted line, SMTZ; blue background, marine sedimentary environment; yellow background, floodplain–estuary depositional conditions; light green to dark blue background, tidal facies to shallow marine environments.

acted on the SMTZ, strengthened SO_4-AOM, and promoted the enrichment of diagenetic framboid particles. However, owing to the consumption of a large amount of sulfate by the enhanced AOM, the sulfate content in the pore water was limited and it was difficult to form gypsum precipitation at this stage.

(b) During the LGM, the entire ECS inner shelf was exposed, including the Zhoushan offshore (Li et al., 2014), resulting in the formation of floodplain and estuary deposits. The organic matter at this time was refractory, which is more difficult to decompose than marine sources (Zhao et al., 2021). The methane content of the upward diffusion was significantly reduced to zero, and the SMTZ subsequently migrated deeper. At this point, the sulfate concentration in the pore water at its original position began to increase. As the SO_4-AOM process advanced, HS^- reacted with reactive Fe in the sediment to produce FeS and release H^+, which was in turn converted into pyrite. H^+ enrichment dissolved carbonates or biological shells, resulting in the enrichment of Ca^{2+} ions. Therefore, it combined with pore-water sulfate in the marine environment to precipitate gypsum, which occurred with pyrite in the SMTZ. Simultaneously, the diagenetic pyrites began to transform into sub-euhedral structures.

(c) Sea level rise after the LGM led to the gradual inundation of continental shelf areas (Lambeck et al., 2014; Li et al., 2014). The study area was influenced by seawater intrusion, and sediments began to form tidal facies deposits under the influence of tidal currents. The formation time of the upper pyrite was later than that of the deeper pyrite; however, the formation mechanism of the pyrites was the same. Organoclastic sulfate reduction may also have occurred, which requires more indicators to be explored. During this stage, the upper pyrite was enriched in the shallow SMTZ; the presence of many tubular pyrites gradually evolved into an irregular microcrystalline euhedral shape close to the deeper position of the paleo-SMTZ. The sedimentary environment was mostly anaerobic, and the anaerobic oxidation of deposited pyrites (Liu et al., 2018b) and the disproportionation reaction of S intermediates (Pirlet et al., 2010) affected the pore water SO_4^{2-}. Simultaneously, the anaerobic oxidation of deposited iron sulfides led to the acidification of local pore water, which in turn led to the dissolution of calcareous biological shells (Pirlet et al., 2010; Liu et al., 2018b; Zhao et al., 2021). The increased Ca^{2+} and SO_4^{2-} content jointly promoted gypsum precipitation.

(d) The sea level tended to be relatively stable. The Holocene mud depocenter then began to develop, forming the present shallow marine environments (Lin et al., 2005). The downward infiltration of seawater may have caused the SO_4-AOM to shift upward and become shallow, forming the current SMTZ position. Spherical pyrite aggregates with smaller diameters, gypsum particles, and the coexistence of pyrite and gypsum were newly formed at the current SMTZ position, which may be related to ongoing SO_4-AOM. The formation mechanism of these authigenic minerals was the same as that in the deep part; however, the formation time was later. Simultaneously, authigenic pyrites in the deeper paleo-SMTZs continued to form and evolve into massive tubular or irregular pyrites. Additional work is needed to confirm the differences in authigenic pyrite in different zones.

5 Conclusion

The morphology and formation mechanisms of authigenic pyrite and gypsum show great potential in tracing depositional

evolution history during the glacial–interglacial cycle in offshore Zhoushan. A variety of authigenic minerals were found in the sediment of core JC-1, which may be related to SO_4-AOM. Thus, the morphology, size distribution, and content of authigenic pyrite in different zones can indicate the evolution of the depositional environment. Additionally, gypsum minerals and the coexistence of pyrite and gypsum were found in the enriched authigenic pyrites at the SMTZs. The sources of sulfate formed by authigenic gypsums may originate from overlying seawater and pyrite oxidation, whereas calcium ions may come from the dissolution of carbonate or calcareous shells caused by local environmental acidification. The results of this study provide a new perspective for better understanding the responses of different sedimentary environments to sea level rise and climate change. However, using coarse-grained heavy minerals to calculate pyrite content may result in bias due to the sorting effect of particle size. In addition, the C-S-Fe cycle in continental shelf sediments is very complex; thus, we only provide a new mineralogy perspective. More detailed work is needed to limit the fate of authigenic minerals. We suggest using multiple indicators, such as ^{34}S isotopes of iron sulfides and/or chemical sequential extraction methods, to obtain the relative contents of various types of iron-bearing minerals in bulk sediments and further explore their potential in tracking sedimentary environment evolution.

Data availability statement

The original contributions presented in the study are included in the article/Supplementary Material. Further inquiries can be directed to the corresponding author.

Author contributions

TS was responsible for manuscript writing and performing tests. KC, YT, and PY provided the study samples. PY revised the text and provided comments. TS and XJ identified the minerals. All authors contributed to the article and approved the submitted version.

Funding

This work was financially supported by the Postdoctoral Foundation of Qingdao (grant QDBSH20220202138), the National Natural Science Foundation of China (grant 42176091), the China-ASEAN Cooperation in Marine Geoscience Research and National Key Research, and Development Plan Project (no. 2019YFE0127200).

Acknowledgments

The authors are grateful to the editors and reviewers for their constructive comments on our manuscript.

Conflict of interest

The authors declare that the research was conducted in the absence of any commercial or financial relationships that could be construed as a potential conflict of interest.

The handling editor JL declared a shared affiliation with the authors TS, KC, PY, XJ, and YT at the time of review.

Publisher's note

Supplementary material

The Supplementary Material for this article can be found online at: https://www.frontiersin.org/articles/10.3389/feart.2023.1165809/full#supplementary-material

References

Amstutz, G. C., Park, W. C., Schot, E. H., and Love, L. G. (1967). Orientation of framboidal pyrite in shale. *Miner. Deposita* 1 (4), 317–321. doi:10.1007/BF00205204

Berner, R. (1984). Sedimentary pyrite formation: An update. *Geochimica Cosmochimica Acta* 48 (4), 605–615. doi:10.1016/0016-7037(84)90089-9

Böttcher, M., and Lepland, A. (2000). Biogeochemistry of sulfur in a sediment core from the west-central Baltic Sea: Evidence from stable isotopes and pyrite textures. *J. Mar. Syst.* 25 (3), 299–312. doi:10.1016/S0924-7963(00)00023-3

Chai, X., Hu, B., Wei, N., Mu, Q., He, J., and He, S. (2015). Distribution, sources and assessment of heavy metals in surface sediments of the Hangzhou Bay and its adjacent areas [J]. *Huanjing Kexue Xuebao/Acta Sci. Circumstantiae* 35, 3906–3916. doi:10.13671/j.hjkxxb.2015.0138

Chang, X., Liu, X., Wang, H., Zhuang, G. C., Ma, Z., Yu, J., et al. (2022). Depositional control on the sulfur content and isotope of sedimentary pyrite from the southeast coast of China since MIS5. *Front. Mar. Sci.* 9, 1005663. doi:10.3389/fmars.2022.1005663

Chang, X., Zhang, M., Gu, Y., Wang, H., and Liu, X. (2020). Formation mechanism and controlling factors of authigenic pyrite in mud sediments on the shelf of the Yellow Sea and the East China Sea (in Chinese with English abstract) [J]. *Chin. J.* 35 (13), 1306–1320. doi:10.11867/j.issn.1001-8166.2020.105

Chen, Q. (1981). Study on authigenic pyrites in sediments of the South huanghai sea [J]. *Acta Geol. Sinica Transl. Chin.* 55 (3), 232–244. doi:10.19762/j.cnki.dizhixuebao.1981.03.007

Chen, S., Sun, J., Shen, C., and Du, X. (2004). Clustered components analysis for functional MRI. *Mar. Geol. Quat. Geol.* 24 (2), 85–98. doi:10.1109/TMI.2003.819922

Chen, Y., Deng, B., and Zhang, J. (2020). Shallow gas in the Holocene mud wedge along the inner East China Sea shelf. *Mar. Petroleum Geol.* 114, 104233. doi:10.1016/j.marpetgeo.2020.104233

Chen, Z., Yan, W., Chen, M. H. J. M. G., and Leung, K. (2007). A simple *in vitro* model to study the stability of acylglucuronides. *Mar. Geol. Quat. Geol.* 27 (2), 91–95. doi:10.1016/j.vascn.2006.03.008

Criddle, A. J. (1974). "A preliminary description of microcrystalline pyrite from the nannoplankton ooze at site 251, Southwest Indian Ocean," in *Proceedings of the Environmental Science, Geology* (London, United Kingdom: Department Of Mineralogy, British Museum (Natural History)). doi:10.2973/DSDP.PROC.26.126.1974

Dantas, R., Hassan, M., Cruz, F., and Jovane, L. (2022). Evidence for methane seepage in South Atlantic from the occurrence of authigenic gypsum and framboidal pyrite in deep-sea sediments. *Mar. Petroleum Geol.* 142, 105727. doi:10.1016/j.marpetgeo.2022.105727

Dong, J., Li, A., Liu, X., Wan, S., Feng, X., Lu, J., et al. (2018). Sea-level oscillations in the East China Sea and their implications for global seawater redistribution during 14.0–10.0 kyr BP. *Palaeogeogr. Palaeoclimatol. Palaeoecol.* 511, 298–308. doi:10.1016/j.palaeo.2018.08.015

Garcia-Gil, S. (2003). A natural laboratory for shallow gas: The Ras Baixas (NW Spain). *Geo-Marine Lett.* 23 (3), 215–229. doi:10.1007/s00367-003-0159-5

Haffert, L., Haeckel, M., Liebetrau, V., Berndt, C., Hensen, C., Nuzzo, M., et al. (2013). Fluid evolution and authigenic mineral paragenesis related to salt diapirism – the Mercator mud volcano in the Gulf of Cadiz. *Geochimica Cosmochimica Acta* 106, 261–286. doi:10.1016/j.gca.2012.12.016

He, X., Tan, L., Duan, X., Yin, P., Xie, Y., Yang, L., et al. (2020). Carbon cycle within the sulfate-methane transition zone in the marine sediments of Hangzhou Bay [J]. *Mar. Geol. Quat. Geol.* 40 (3), 51–60. doi:10.16562/j.cnki.0256-1492.2020021401

Hu, X., Gu, Z., Zhang, X., Zhao, L., Xing, Z., Liu, C., et al. (2016). Development of a novel monoclonal antibody to human inducible co-stimulator ligand (ICOSL): Biological characteristics and application for enzyme-linked immunosorbent assay. *Mar. Geol. Quat. Geol.* 36 (1), 151–157. doi:10.1016/j.intimp.2016.04.019

Jiang, W., Cao, K., Duan, X., He, X., Yin, P., Chen, J., et al. (2023). Influence of sedimentary environment evolution on fingerprint characteristics of methane isotopes: A case study from hangzhou bay. *J. Geophys. Res. Biogeosciences* 128, 1–14. doi:10.1029/2022JG007357

Jørgensen, B. B. (1982). Mineralization of organic matter in the sea bed—the role of sulphate reduction. *Nature* 296 (5858), 643–645. doi:10.1038/296643a0

Kang, X., Liu, S., and Zhang, G. (2014). Reduced inorganic sulfur in the sediments of the Yellow Sea and East China sea. *Acta Oceanol. Sin.* 33 (9), 100–108. doi:10.1007/s13131-014-0499-1

Lambeck, K., Rouby, H., Purcell, A., Sun, Y., and Sambridge, M. (2014). Sea level and global ice volumes from the last glacial maximum to the Holocene. *Proc. Natl. Acad. Sci. U. S. A.* 111 (43), 15296–15303. doi:10.1073/pnas.1411762111

Li, G., Li, P., Liu, Y., Qiao, L., Ma, Y., Xu, J., et al. (2014). Sedimentary system response to the global sea level change in the East China Seas since the last glacial maximum. *Earth-Science Rev.* 139, 390–405. doi:10.1016/j.earscirev.2014.09.007

Lin, C., Gu, L., Li, G., Zhao, Y., and Jiang, W. (2004). Geology and formation mechanism of late Quaternary shallow biogenic gas reservoirs in the Hangzhou Bay area, eastern China. *Aapg Bull. - AAPG Bull.* 88 (5), 613–625. doi:10.1306/01070403038

Lin, C. M., Li, Y. L., Zhuo, H. C., Shurr, G., Ridgley, J., Zhang, Z. P., et al. (2010). Features and sealing mechanism of shallow biogenic gas in incised valley fills (the Qiantang River, eastern China): A case study. *Mar. Petroleum Geol.* 27 (4), 909–922. doi:10.1016/j.marpetgeo.2009.11.006

Lin, C-M., Zhuo, H-C., and Gao, S. (2005). Sedimentary facies and evolution in the Qiantang River incised valley, eastern China. *Mar. Geol.* 219 (4), 235–259. doi:10.1016/j.margeo.2005.06.009

Lin, Q., Wang, J., Su, P., and Hu, G. (2016a). Formation mechanism of authigenic gypsum in marine methane hydrate settings: Evidence from the northern South China Sea. *Deep Sea Res. Part I Oceanogr. Res. Pap.* 115, 210–220. doi:10.1016/j.dsr.2016.06.010

Lin, Q., Wang, J., Sun, F., and Lin, R. (2016b). Enhanced framboidal pyrite formation related to anaerobic oxidation of methane in the sulfate-methane transition zone of the northern South China Sea. *Mar. Geol.* 379, 100–108. doi:10.1016/j.margeo.2016.05.016

Lin, Z., Lu, Y., Xu, L., Gong, J., Lu, H., Teichert, B., et al. (2016c). Stable isotope patterns of coexisting pyrite and gypsum indicating variable methane flow at a seep site of the Shenhu area, South China Sea. *J. Asian Earth Sci.* 123, 213–223. doi:10.1016/j.jseaes.2016.04.007

Lin, Z., Peckmann, J., Lu, Y., Xu, L., Strauss, H., Zhou, H., et al. (2016d). How sulfate-driven anaerobic oxidation of methane affects the sulfur isotopic composition of pyrite: A sims study from the South China sea. *Chem. Geol.* 440, 26–41. doi:10.1016/j.chemgeo.2016.07.007

Lin, Z., Strauss, H., Lu, Y., Gong, J., Xu, L., Lu, H., et al. (2017). Multiple sulfur isotope constraints on sulfate-driven anaerobic oxidation of methane: Evidence from authigenic pyrite in seepage areas of the South China Sea. *Geochimica Cosmochimica Acta* 211, 153–173. doi:10.1016/j.gca.2017.05.015

Lin, Z., Sun, X., Yang, L., and Xu, L. (2012). Formation mechanism of authigenic gypsum in marine methane hydrate settings: Evidence from the northern South China Sea [J]. *Mineral. Deposits* 115 (31), 1–2. doi:10.16111/j.0258-7106.2012.s1.218

Liu, X., Fike, D., Li, A., Dong, J., Xu, F., Zhuang, G. C., et al. (2019). Pyrite sulfur isotopes constrained by sedimentation rates: Evidence from sediments on the East China Sea inner shelf since the late Pleistocene. *Chem. Geol.* 505, 66–75. doi:10.1016/j.chemgeo.2018.12.014

Liu, X., Li, A., Dong, J., Lu, J., Huang, J., and Wan, S. (2018a). Provenance discrimination of sediments in the Zhejiang-Fujian mud belt, East China Sea: Implications for the development of the mud depocenter. *J. Asian Earth Sci.* 151, 1–15. doi:10.1016/j.jseaes.2017.10.017

Liu, X., Li, A., Dong, J., Zhuang, G-C., Xu, F., and Wan, S. (2018b). Nonevaporative origin for gypsum in mud sediments from the East China Sea shelf. *Mar. Chem.* 205, 90–97. doi:10.1016/j.marchem.2018.08.009

Liu, X., Li, A., Fike, D., Dong, J., Xu, F., Zhuang, G. C., et al. (2020a). Environmental evolution of the East China Sea inner shelf and its constraints on pyrite sulfur contents and isotopes since the last deglaciation. *Mar. Geol.* 429, 106307. doi:10.1016/j.margeo.2020.106307

Liu, X., Li, A., Ma, Z., Dong, J., Zhang, K., Xu, F., et al. (2020b). Constraint of sedimentary processes on the sulfur isotope of authigenic pyrite (in Chinese with English abstract) [J]. *Chin. J.* 38 (1), 124–137. doi:10.14027/j.issn.1000-0550.2019.073

Liu, X., Zhang, M., Li, A., Dong, J., Zhang, K., Gu, Y., et al. (2022). Sedimentary pyrites and C/S ratios of mud sediments on the East China Sea inner shelf indicate late Pleistocene-Holocene environmental evolution. *Mar. Geol.* 450, 106854. doi:10.1016/j.margeo.2022.106854

Liu, X., Zhang, M., Li, A., Fan, D., Dong, J., Jiao, C., et al. (2021). Depositional control on carbon and sulfur preservation onshore and offshore the Oujiang Estuary: Implications for the C/S ratio as a salinity indicator. *Cont. Shelf Res.* 227, 104510. doi:10.1016/j.csr.2021.104510

Love, L. G., and Amstutz, G. C. (1966). Review of microscopic pyrite from the devonian chattanooga shale and rammelsberg banderz [J]. *Fortschr Mineral.* 43, 273–309.

Miao, X., Feng, X., Liu, X., Li, J., and Wei, J. (2021). Effects of methane seepage activity on the morphology and geochemistry of authigenic pyrite [J]. *Mar. Petroleum Geol.* 133, 105231. doi:10.1016/j.marpetgeo.2021.105231

Middelburg, J., and Nieuwenhuize, J. (1998). Carbon and nitrogen stable isotopes in suspended matter and sediments from the Schelde Estuary. *Mar. Chem.* 60 (3), 217–225. doi:10.1016/S0304-4203(97)00104-7

Ni, Y., Dai, J., Zou, C., Liao, F., Shuai, Y., and Zhang, Y. (2013). Geochemical characteristics of biogenic gases in China. *Int. J. Coal Geol.* 113, 76–87. doi:10.1016/j.coal.2012.07.003

Pirlet, H., Wehrmann, L., Brunner, B., Frank, N., Jan, D., Rooij, D., et al. (2010). Diagenetic formation of gypsum and dolomite in a cold-water coral mound in the Porcupine Seabight, off Ireland: Diagenetic gypsum in a cold-water coral mound. *Sedimentology* 57 (3), 786–805. doi:10.1111/j.1365-3091.2009.01119.x

Richardson, J., Keating, C., Lepland, A., Hints, O., Bradley, A., and Fike, D. (2019). Silurian records of carbon and sulfur cycling from Estonia: The importance of depositional environment on isotopic trends. *Earth Planet. Sci. Lett.* 512 (4), 71–82. doi:10.1016/j.epsl.2019.01.055

Rickard, D., and Luther, G. (2007). Chemistry of iron sulfides. *Chem. Rev.* 107 (2), 514–562. doi:10.1021/cr0503658

Rickard, D., Mussmann, M., and Steadman, J. (2017). Sedimentary sulfides. *Sediment. Sulfides J. Elem.* 13 (2), 117–122. doi:10.2113/gselements.13.2.117

Rickard, D. (2012). "Sulfidic sediments and sedimentary rocks," in *Developments in Sedimentology*. School of Earth and Ocean Sciences Cardiff University Wales (United Kingdom: Elsevier), 767–801. doi:10.1016/B978-0-444-52989-3.20001-9

Shevelkova, A. N., Sal'nikov, Y. I., Kuz'mina, N. L., Ryabov, A., Wilkin, R., Barnes, H. L., et al. (1996). The size distribution of framboidal pyrite in modern sediments: An indicator of redox conditions. *Geochimica Cosmochimica Acta* 60 (20), 3897–3912. doi:10.1016/0016-7037(96)00209-8

Siesser, W. G., and Rogers, J. J. S. (1976). Authigenic pyrite and gypsum in South West African continental slope sediments. *Environ. Sci. Geogr. Geol.* 23, 567–577. doi:10.1111/J.1365-3091.1976.TB00068.X

Sun, X., Fan, D., Liao, H., and Tian, Y. (2020). Fate of organic carbon burial in modern sediment within Yangtze River estuary. *J. Geophys. Res. Biogeosciences* 125 (2), 1–20. doi:10.1029/2019JG005379

Taylor, K., and Macquaker, J. (2011). Iron minerals in marine sediments record chemical environments. *Elements* 7 (2), 113–118. doi:10.2113/gselements.7.2.113

Vijaykumar, P., and Vaz, G. (1995). Occurrence of authigenic gypsum in a deep sea core off Madras [J]. *J. - Geol. Soc. India* 45, 483–486.

Vogel, M., Des Marais, D., Parenteau, M., Jahnke, L., Turk-Kubo, K., and Kubo, M. (2010). Biological influences on modern sulfates: Textures and composition of gypsum deposits from Guerrero Negro, Baja California Sur, Mexico [J]. *Sediment. Geol. - Sediment. Geol.* 223 (3), 265–280. doi:10.1016/j.sedgeo.2009.11.013

Wu, Y., Dittmar, T., Ludwichowski, K-U., Kattner, G., Zhang, J., Zhu, Z., et al. (2007). Tracing suspended organic nitrogen from the Yangtze River catchment into the East China sea. *Mar. Chem.* 107, 367–377. doi:10.1016/j.marchem.2007.01.022

Wu, Y., Eglinton, T., Yang, L., Deng, B., Montluçon, D., and Zhang, J. (2013). Spatial variability in the abundance, composition, and age of organic matter in surficial sediments of the East China sea: Spatial variability in the abundance. *J. Geophys. Res. Biogeosciences* 118, 1495–1507. doi:10.1002/2013jg002286

Yang, Z., Guo, R., Shi, X., He, S., Wang, L., Dai, M., et al. (2016). Bioaugmentation of Hydrogenispora ethanolica LX-B affects hydrogen production through altering indigenous bacterial community structure [J]. *Bioresour. Technol.* 211, 97. doi:10.1016/j.biortech.2016.03.097

Yuan, H-W., Chen, J., Ye, Y., Lou, Z. H., Jin, A. M., Chen, X. G., et al. (2017). Sources and distribution of sedimentary organic matter along the Andong salt marsh, Hangzhou Bay. *J. Mar. Syst.* 174, 78–88. doi:10.1016/j.jmarsys.2017.06.001

Zhao, B., Yao, P., Bianchi, T., and Yu, Z. (2021a). Controls on organic carbon burial in the eastern China marginal seas: A regional synthesis. *Glob. Biogeochem. Cycles* 35 (4), 1–27. doi:10.1029/2020GB006608

Zhao, J., Wang, J., Phillips, S., Liang, J., Su, P., Lin, Q., et al. (2021b). Non-evaporitic gypsum formed in marine sediments due to sulfate-methane transition zone fluctuations and mass transport deposits in the northern South China Sea. *Mar. Chem.* 233, 103988. doi:10.1016/j.marchem.2021.103988